Title

Noncontrast enhanced four-dimensional dynamic MRA with golden angle radial acquisition and k-space weighted image contrast (KWIC) reconstruction

Journal

Magnetic Resonance in Medicine, 72(6)

ISSN

0740-3194

Authors

Song, Hee Kwon
Yan, Lirong
Smith, Robert X
et al.

Publication Date

2014-12-01

DOI

10.1002/mrm.25057

Peer reviewed

FULL PAPER

Magnetic Resonance in Medicine 00:00–00 (2013)

Noncontrast Enhanced Four-Dimensional Dynamic MRA with Golden Angle Radial Acquisition and K-space Weighted Image Contrast (KWIC) Reconstruction

Hee Kwon Song,[1]* Lirong Yan,[2] Robert X. Smith,[2] Yiqun Xue,[1] Stanislas Rapacchi,[3] Subashini Srinivasan,[3,4] Daniel B. Ennis,[3,4] Peng Hu,[3] Nader Pouratian,[5] and Danny J.J. Wang[2,3]

Purpose: To explore the feasibility of 2D and 3D golden-angle radial acquisition strategies in conjunction with k-space weighted image contrast (KWIC) temporal filtering to achieve noncontrast enhanced dynamic MRA (dMRA) with high spatial resolution, low streaking artifacts and high temporal fidelity.

Methods: Simulations and in vivo examinations in eight normal volunteers and an arteriovenous malformation patient were carried out. Both 2D and 3D golden angle radial sequences, preceded by spin tagging, were used for dMRA of the brain. The radial dMRA data were temporally filtered using the KWIC strategy and compared with matched standard Cartesian techniques.

Results: The 2D and 3D dynamic MRA image series acquired with the proposed radial techniques demonstrated excellent image quality without discernible temporal blurring compared with standard Cartesian based approaches. The image quality of radial dMRA was equivalent to or higher than that of Cartesian dMRA by visual inspection. A reduction factor of up to 10 and 3 in scan time was achieved for 2D and 3D radial dMRA compared with the Cartesian-based counterparts.

Conclusion: The proposed 2D and 3D radial dMRA techniques demonstrated image quality comparable or even superior to those obtained with standard Cartesian methods, but within a fraction of the scan time. **Magn Reson Med 000:000–000, 2013. © 2013 Wiley Periodicals, Inc.**

Key words: dynamic MRA; KWIC; golden angle; radial MRI

INTRODUCTION

The evaluation of dynamic flow patterns within the cerebrovasculature is useful for several clinical indications, such as steno-occlusive disease, arteriovenous malformation (AVM), and cerebral aneurysm. As the gold standard, digital subtraction angiography (DSA) can provide images of the cerebral blood circulation with both high temporal and spatial resolution. However, as an invasive technique, DSA exposes both doctors and patients to certain known risks including: ionizing radiation exposure, thromboembolic events, puncture of the femoral artery, catheter placement complications, iodinated contrast agent reactions and operator dependent errors (1).

Existing contrast enhanced dynamic MRA (CE-dMRA) techniques enable acquisitions with sub-millimeter spatial resolution and/or sub-second temporal resolution, which can rival those of DSA. The improvements in the temporal and spatial resolution of CE-dMRA can be largely attributed to recent advances in fast imaging techniques such as undersampled back projection, view sharing, keyhole and parallel imaging (2–10). To date, however, it remains challenging to obtain both high temporal and spatial resolution in the same acquisition using CE-dMRA (11,12). The technique also requires intravenous injection of contrast agents, which introduces additional risks and costs and limits use in subjects with poor renal function.

Recently, noncontrast enhanced time-resolved 4D dynamic MRA was introduced by combining arterial spin labeling (ASL) with a segmented multiphase TrueFISP readout (13,14). Initial feasibility studies demonstrated the capability of this technique to provide a temporal resolution of 50–100 ms and a spatial resolution of (1 to 1.25 mm)^3 in the evaluation of AVM (15,16) and steno-occlusive diseases (17). However, to perform 4D dMRA within a clinically acceptable time, tradeoffs have to be made between the number of time frames, spatial resolution, and/or volumetric coverage of the regions of interest in existing 4D dMRA based on Cartesian trajectories.

Dynamic radial acquisition with a golden angle view increment is a recent development for 4D dynamic MRI (18). Subsequent radial profiles are separated by the golden angle (111.246°) which is optimal for flexible image reconstruction from an arbitrary number of profiles in radial MRI, allowing advanced sliding window reconstructions. Dynamic golden angle radial acquisition can be further combined with k-space weighted image

[1]Department of Radiology, University of Pennsylvania Medical Center, Philadelphia, Pennsylvania, USA.

[2]Laboratory of Functional MRI Technology (LOFT), Ahmanson-Lovelace Brain Mapping Center, Department of Neurology, UCLA, Los Angeles, California, USA.

[3]Department of Radiological Sciences, UCLA, Los Angeles, California, USA.

[4]Department of Bioengineering, UCLA, Los Angeles, California, USA.

[5]Department of Neurosurgery, UCLA, Los Angeles, California, USA

Grant sponsor: NIH; Grant numbers: P41-EB015893, R01-MH080892, R01-NS081077, R01-EB014922.

*Correspondence to: Hee Kwon Song, Ph.D., Hospital of the University of Pennsylvania, Department of Radiology, 1 Silverstein / MRI, 3400 Spruce Street, Philadelphia, PA 19104. E-mail: hsong@uphs.upenn.edu

Additional Supporting Information may be found in the online version of this article.

Received 23 May 2013; revised 30 October 2013; accepted 4 November 2013

DOI 10.1002/mrm.25057

Published online 00 Month 2013 in Wiley Online Library (wileyonlinelibrary.com).

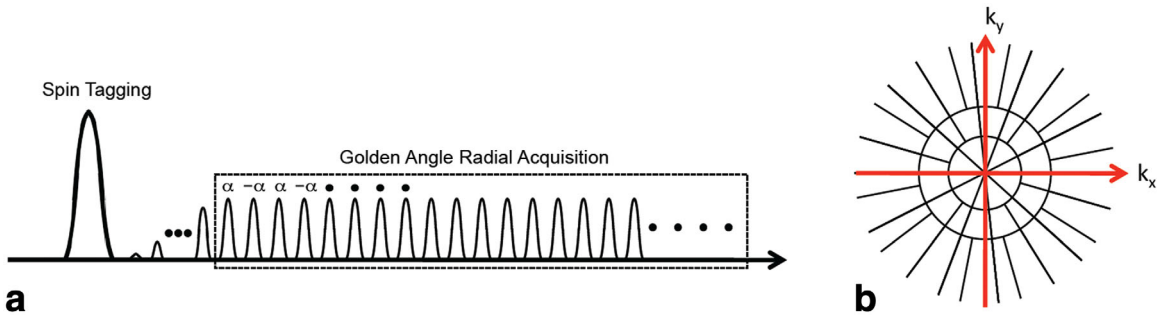

FIG. 1. **a**: The dynamic golden angle radial sequence with a FAIR spin tagging preparation. Each radial acquisition line is based on a balanced steady-state (TrueFISP) readout with golden angle increment ($\theta_g = 111.246°$) between successive radial k-space lines. A series of 20 linearly increasing amplitude RF pulses were used for catalyzation. **b:** An example KWIC reconstruction strategy used to enhance the effective temporal resolution of the dynamic series. Fewer views are encoded at k-space center (20 in our study), while the outer regions are encoded by increasing greater numbers of views. [Color figure can be viewed in the online issue, which is available at wileyonlinelibrary.com.]

contrast (KWIC) (19,20) to achieve both high spatial and temporal resolution while preserving image quality. In KWIC, the central k-space (which primarily determines the image contrast) is sampled by the radial views of the time frame of interest, while peripheral k-space regions include radial views of neighboring time frames (similar to view sharing). The present study explored the feasibility of 2D single- and angle-interleaved multi-shot, as well as 3D stack-of-stars, golden-angle radial acquisition strategies followed by temporal filtering using KWIC to achieve 4D dMRA with high image quality and spatial resolution, as well as high temporal fidelity.

METHODS

Simulation

Simulations were first carried out to evaluate whether radial data acquisition and KWIC filtering can potentially lead to temporal smoothing on the measured dMRA signal. To this end, vessels of various lumen sizes were simulated by subtracting two analytically generated k-space data of concentric circles of different radii. The inner circle diameter was kept constant at 76 mm, while that of the outer was varied to yield vessel thickness ranging from 1 to 5 mm (21). The vessels were modeled as rings so that the measurements reflect an average of all possible in-plane vessel orientations, and also so that any partial volume effects arising from small vessel sizes are averaged. For the dMRA signal time curve, a gamma variate model described by MacIntosh et al (22) was implemented with slightly adjusted parameters to more closely resemble our observed dMRA time courses (full-width-at-half-max (FWHM) of the time-intensity curve $\sim$ 800 ms):

$$S(t) = \frac{A}{rTTP^{sh \cdot rTTP}} \cdot (t - t_0)^{sh \cdot rTTP} \cdot \exp\left(-sh \cdot [(t - t_0) - rTTP]\right) \quad [1]$$

where A = relative amplitude (1.0); $rTTP$ = relative time to peak (0.7 s); sh = sharpness (6.0 s^{-1}); and t_0 = bolus arrival time (0.7 s).

The imaging parameters were similar to those used in vivo: FOV = 256 mm, 256 points per readout, TR = 4.58 ms, 750 views with golden angle increment per shot, number of shots = 1, 2, 4, and 8. For single-shot acquisition, dynamic radial sampling with view angle increment of θ_g=111.246° (golden angle) (18) was used. For the multi-shot version of the golden angle sequence, the starting view angle was $(n\text{-}1)\cdot\theta_g$ for shot #n and for each shot the view angles were incremented by $N_s \cdot \theta_g$, where N_s is the total number of shots. This scheme permits a multi-shot acquisition while still providing the flexibility of the golden angle scheme in which the number of views used during reconstruction is flexible. The simulated data were reconstructed using the KWIC strategy in a similar manner as the in vivo data, which is described in more detail below. A region-of-interest (ROI) mask was generated from the peak intensity image of each dynamic series by thresholding to 50% of the maximum value of the peak dMRA signal. The ROIs were used to make the dynamic time series measurements, and FWHM values were subsequently computed from the simulated signal time course.

Pulse Sequences

As an initial step, a dMRA pulse sequence was developed using 2D radial acquisitions that allowed single- and angle-interleaved multi-shot acquisitions. The purpose was to evaluate the potential effect of temporal blurring caused by single and multi-shot radial acquisitions on the dMRA time courses. The 2D dMRA pulse sequence consisted of continuous TrueFISP readout following slice-selective or nonselective inversion pulses, as in FAIR (23) (Fig. 1). Single and multi-shot acquisition schemes were carried out as described above for the simulation experiments. Imaging parameters were as follows: FOV = 256 mm, 256 points per readout, TR = 4.58 ms, TE = TR/2, 500 views per shot, flip angle (FA) = 30°, bandwidth (BW) = 630Hz/pixel, ten 4-mm slices covering the Circle of Willis and main branches, scan time = N_s × 1 min. For comparison, a 2D Cartesian version of the dMRA sequence was evaluated with closely matched imaging parameters. Twenty-two phases (10 shots) with a temporal resolution of 105 ms were acquired to cover the volume within a scan time of 10 min. Imaging parameters for the Cartesian sequences were as follows: FOV = 256 × 256 mm^2, matrix = 256 × 256, BW = 630 Hz/pixel, FA = 30°, TR = 4.42 ms, TE = TR/2.

A 3D version of the dMRA sequence was subsequently developed by using radial stack-of-stars sampling (5). The pulse sequence comprised identical preparation prepulses and similar imaging parameters as for the single-shot 2D acquisition (except with slightly longer TR = 4.7 ms and FA = 25°). Two 3D radial dMRA scans were performed covering the Circle of Willis and main branches: one with 32 × 1.5 mm slices acquired within a scan time of 3 min, and another with 64 × 1 mm slices (1 × 1 × 1 mm^3 isotropic spatial resolution) acquired within a scan time of 6 min. Both had an effective temporal resolution of 94 ms. For comparison, a 3D Cartesian version of the dMRA sequence was also evaluated with closely matched imaging parameters. Thirty phases with a temporal resolution of 80 ms covering a 3D slab of 32 × 1.5 mm sections (with GRAPPA = 2 acceleration along the phase-encoding direction) were acquired within a total scan time of 10 min. Imaging parameters were as follows: FOV = 256 × 192 mm^2, matrix = 256 × 192, BW = 849Hz/pixel, FA = 25°, TR = 3.96 ms, TE = TR/2, and 7/8 partial k-space acquisition along the slice-encoding direction (used only for 3D Cartesian acquisition).

MRI Experiment

Eight healthy volunteers (31 ± 5 years, 3 females and 5 males) were recruited for the in vivo evaluation of the proposed dMRA sequences after providing written informed consent. Subjects were scanned on a Siemens Tim Trio 3.0T MRI system using a body coil transmitter and a product 12-channel head coil receiver with imaging parameters described above.

In addition, one patient with a Spetzler-Martin grade-V AVM (20 years, female) was imaged with the 3D stack-of-stars radial dMRA and 3D Cartesian dMRA protocols. The imaging parameters for the 3D radial dMRA sequence were identical to those used in healthy volunteers. Due to time limitations, the in-plane resolution of 3D Cartesian dMRA was slightly decreased to 1.1 × 1.1 mm^2 (FOV = 220 × 165 mm^2, matrix = 192 × 144). Other parameters were identical to those used in healthy volunteers.

Image Reconstruction

Following data acquisition, raw k-space data were transferred to a workstation offline and the dMRA image series reconstructed using custom MATLAB programs (MathWorks, Natick, MA). For the 3D stack-of-stars radial data, a Fourier transform along the slice-encoding direction was applied to separate the individual slices. Both 2D and 3D datasets for each slice were reconstructed using 160 total views per time frame (total temporal footprint per time frame ~750 ms), with an effective temporal resolution of 92 ms (2D) or 94 ms (3D) by means of the KWIC filter (19,20). The choice of ~100 ms temporal resolution was based on our past experience performing Cartesian dMRA in AVM patients and healthy volunteers (14,15). KWIC exploits the oversampling of the k-space center in the radial acquisition by using drastically fewer views in the central region of k-space. In this study, 20 views from each shot were used in the center-most region. This reduction accommodates a proportionately larger increase in effective temporal resolution because image contrast is determined primarily by the signal in the central k-space region. Progressively larger numbers of views were used toward the outer k-space regions (Fig. 1b).

In the current implementation of the KWIC reconstruction strategy, we chose to increase the number of views by twice the number which encode the central k-space region in subsequent adjacent k-space regions, with the transition radius determined by the Nyquist criterion. So for the single shot dataset, 20 views were used at center, 40 more views are added in the adjacent annular region for a total of 60. The next outer region would have 100, and so on. Our chosen strategy also allowed for the addition of fewer than 40 views in the outer-most annulus region to permit arbitrary number of total views to be used in each time frame. For 2D multi-shot radial acquisitions, the number of central k-space views was multiplied by the number of shots, and as above, twice that number is added to subsequent annular regions, with the transition radius adjusted according to Nyquist requirements. The eight-shot acquisition did not require KWIC filtering because using 20 views/shot provided all 160 views. The VORONOI algorithm was used to weight each k-space point before regridding (24).

Following the reconstruction of all slices, slice-selective (label) and nonselective (control) image series were subtracted and maximum-intensity projection (MIP) images along the axial plane were subsequently created. For Cartesian based scans, magnitude images reconstructed on the scanner were used for generating dMRA images by subtraction between label and control acquisitions, followed by MIP for each temporal phase along the axial direction. In addition, for 3D acquisitions MIP images were also created along coronal and sagittal planes.

Quantitative Image Analysis

For signal-to-noise ratio (SNR) and contrast-to-noise (CNR) measurements, a MIP image corresponding to signal peak in each series was zoomed 2× and a 25 × 12 rectangular region-of-interest was drawn covering the M1 vessel and the adjacent background. The top 25 highest-intensity pixels were then averaged to determine the mean signal. This was done to minimize underestimation of signal intensities due to partial volume effects. Standard deviations of these pixel intensities were also computed. Average noise level was determined by taking the standard deviation of a large background ROI placed away from the brain, ensuring the complete absence of any motion- or reconstruction-related artifacts. To determine CNR, the M1 vessel pixels used for SNR measurements were subtracted by the residual brain tissue signal, which was measured with a large irregularly shaped ROI placed in a region of the MIP image between the middle and posterior cerebral arteries where vessels were absent. The resulting signal differences were divided by the measured noise and subsequently averaged.

To measure the dynamic signal intensity curves of the MCA in the 2D acquisitions, small ROIs encompassing the MCA vessel were manually drawn. For 3D, the dynamic time intensity curves of the dMRA signal were measured in different segments of the cerebral arteries

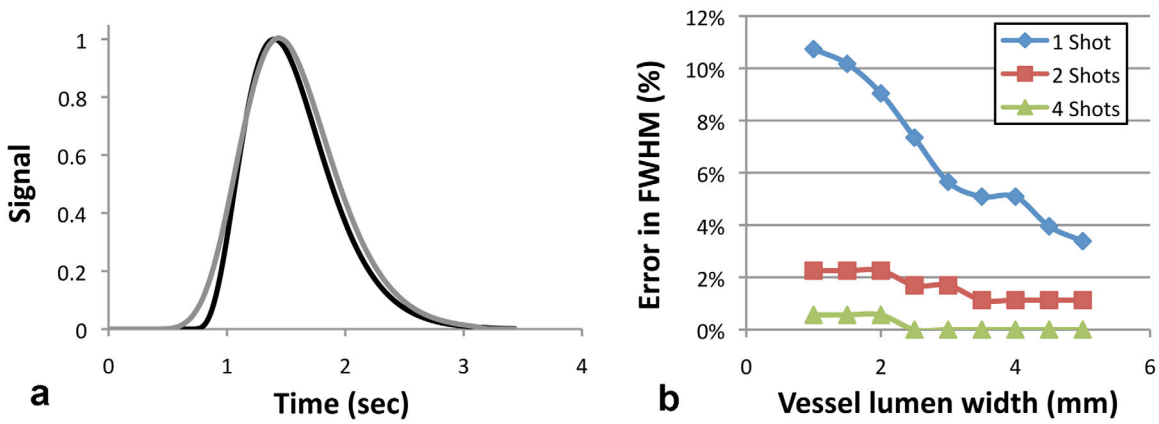

FIG. 2. **a**: Simulation results comparing true vessel signal enhancement (black) to that of KWIC-reconstruction (gray) for a vessel of 1 mm diameter (1 pixel). **b:** Effects of vessel lumen size on full-width-at-half-maximum (FWHM) of the dynamic time course. Errors in FWHM for the 8-shot images were essentially zero (at 0.5% precision). [Color figure can be viewed in the online issue, which is available at wileyonlinelibrary.com.]

using the following procedure: An intensity threshold level was first determined visually for each MIP series by ensuring that the intensities of the smallest visible vessels in the images were above the threshold. The chosen threshold was then applied to that image series and pixels below the threshold were removed from analysis, while those above the threshold maintained their value. Five ROIs encompassing different vascular regions (M1, M2, M3/M4, P1/P2, P3) were drawn by an experienced reader and the average signal time course curves for those regions were measured.

Evaluation of Image Quality

The 3D radial and Cartesian dMRA datasets (both at $1 \times 1 \times 1.5$ mm^3 resolution) of healthy volunteers were blindly and independently reviewed by 2 raters (one MRA expert with >5 years experience (S.R.) and one neurosurgeon (N.P.)) according to a 4-point Likert-like rating scale (25) to assess image quality on 9 vessel segments of each subject (ACA; left and right M1, M2 and M3/4; P1/2 and P3). Statistical analysis was carried out using STATA 13.0 software (College Station, TX). The Wilcoxon signed rank test was performed to compare the mean ratings of image quality of radial and Cartesian dMRA in each vessel segment respectively.

RESULTS

Simulation Results

Results of the simulation study are shown in Figure 2. Figure 2a plots the "true" dMRA signal in a 1 mm (1 pixel) thick vessel along with the signal detected from a single-shot radial acquisition followed by KWIC reconstruction. The measured time course closely follows the true signal, albeit with a slight broadening of the curve. Even for such a small vessel, the FWHM is overestimated only by approximately 10.7%. Figure 2b plots the vessel lumen width vs. relative error of the FWHM of the dMRA signal time course for the different numbers of shots, demonstrating that the temporal broadening due to KWIC reconstruction is typically less than approximately 5% except for the smallest of the vessels of the single-shot acquisition. These results demonstrate that the KWIC strategy generally does not substantially affect the measured time course of the dynamic MRA signal.

Comparison of 2D Radial and Cartesian dMRA

Figure 3 shows the dMRA MIP images of a normal volunteer at six phases using the 2D radial acquisition with different numbers of shots, as well as the Cartesian images. Dynamic filling of small branches of middle cerebral artery (MCA) and posterior cerebral artery (PCA) is clearly visualized for all acquisitions. The image quality is largely consistent between the two sampling schemes, although ghosting artifacts, likely due to cardiac pulsation, can be seen along the midsagittal plane in the Cartesian images. The average SNR (±SD) of the MCA in the healthy volunteers for the radial acquisition was consistent for the different numbers of shots, ranging from 35.6 (±7.0) to 39.8 (±4.4) and the CNR from 29.6 (±2.3) to 33.7 (±4.3), while the SNR and CNR for Cartesian were 28.7 (±6.9) and 24.3 (±6.8), respectively. Figure 4 depicts the signal time course in the MCA of one of the subjects, demonstrating good agreement among the Cartesian and radial techniques.

Evaluation of 3D Radial and Cartesian dMRA

Figure 5 shows the dMRA MIP images at seven phases using 32-slice 3D single shot radial (a) and corresponding Cartesian (b) acquisitions. The dynamic blood flow pattern through the Circle of Willis and its main branches can be clearly visualized by radial dMRA, including small distal branches of the MCA and PCA. The background tissue signal was markedly suppressed in radial dMRA, resulting in sharp MRA images for all temporal phases. The average SNR and CNR of the radial data of healthy volunteers were 65.7 (±7.7) and 58.1 (±8.1), respectively, and those of Cartesian were 92.4 (±9.6) and 83.5 (±9.7). The SNR and CNR for the isotropic 64-slice radial sequence were 47.0 (±3.8) and 38.0 (±3.8), respectively. The $1 \times 1 \times 1$ mm^3 isotropic spatial resolution enabled high quality MIP dMRA images to

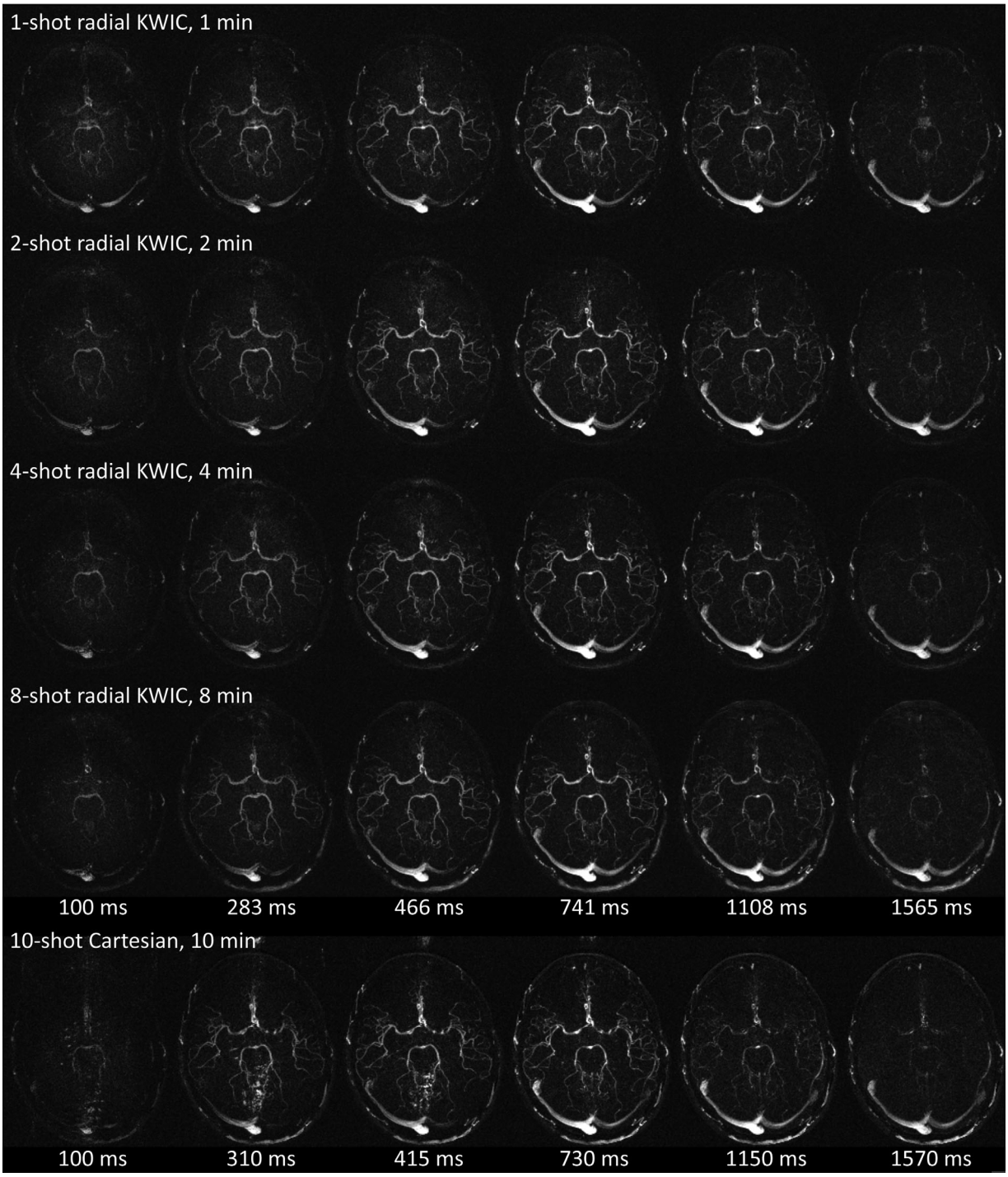

FIG. 3. 2D radial dMRA MIP images at six phases reconstructed using different numbers of shots, compared with the Cartesian acquisition.

be generated for sagittal, coronal and axial views (see Fig. 6).

Figure 7 compares the dMRA signal time courses from five vascular ROIs of 32- and 64-slice 3D radial sequences. Those of Cartesian dMRA are also shown for comparison. The figure clearly demonstrates that the 3D radial sequence provides the signal time course in the various branches of the cerebral arteries. The slight delay in location of the peak signal in the smaller branches (M3/4 and P3) can also be seen compared with their larger upstream arteries.

Table 1 shows the image quality ratings comparing radial and Cartesian dMRA image series in the healthy volunteers. The weighted Kappa was calculated to be 0.74 which indicated a good level of inter-rater consistency. Ratings ranged from moderate ($\sim$2) to excellent (4), and the results show that radial images scored equivalent to or better than the Cartesian counterpart. Out of the nine vessel segments,

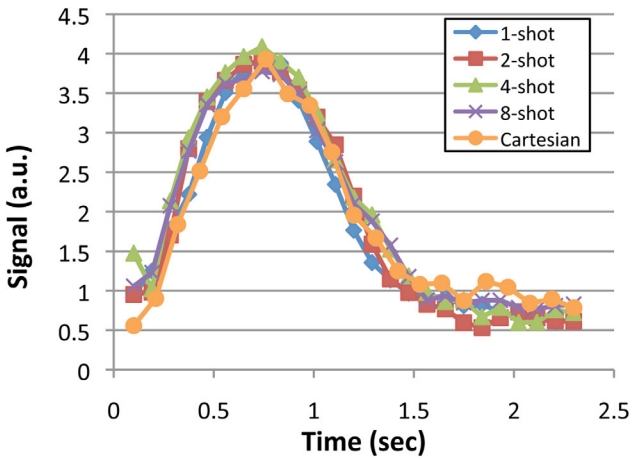

FIG. 4. Normalized MCA time courses of 2D radial and Cartesian based dMRA for one of the subjects. [Color figure can be viewed in the online issue, which is available at wileyonlinelibrary.com.]

the image quality of radial acquisition was significantly higher in one segment (P3), while in several others the improvements did not reach statistical significance.

Dynamic MRA in AVM

Figure 8 displays six time frames of the 32 slice radial dMRA MIP images of the AVM patient, along with the corresponding Cartesian images. The AVM measures approximately 6.1 × 4.9 × 4.9 cm (red circles), has no associated aneurysms, is fed by multiple dilated vessels from the right MCA (pink arrow) and left ACA branches, and demonstrates early venous drainage through the straight sinus (yellow arrow) as well as later drainage through superficial cerebral veins into the sagittal sinus (blue arrow). The 3D stack-of-stars radial dMRA provides a sharper and effectively higher resolution image of the AVM than the 3D Cartesian dMRA. As such, there is greater visualization of extra-nidal vessels (e.g., PCA territory), which does not distract from the delineation of the AVM. While there is slight temporal blurring relative to the 3D Cartesian dMRA, the radial dMRA maintains more than sufficient temporal resolution to clinically demonstrate the dynamic nature of the filling and drainage of the AVM (see movie files included in Supplemental Information).

DISCUSSION

The present study demonstrates the feasibility of fast 4D dynamic MRA using 2D and 3D golden angle radial acquisitions in conjunction with KWIC reconstruction. The image quality was comparable to corresponding Cartesian-based dMRA scans without noticeable streaking artifacts. In addition, both simulations and experimental data demonstrated that the proposed radial dMRA is able to achieve a high temporal resolution (~100 ms/frame) without significant temporal blurring, requiring only a fraction of the scan time compared with that of standard Cartesian-based methods. This scan time reduction could prove to be valuable in patient studies, particularly in visualizing the smaller vascular structures in which even small amount of motion could render them difficult to distinguish. Radial acquisitions are also known to be more robust to motion artifacts (26), such as cardiac pulsations, where artifacts are typically dispersed throughout the entire imaging slice, while that of Cartesian sequences appear along the phase-encoding direction, often resulting in more prominent image artifacts. Background signal may also be better cancelled in the subtraction image due to greater similarities between two images even in the presence of varying motion.

Sufficiently high SNR and CNR were achieved with both 2D and 3D radial acquisitions despite the substantially reduced scan times (from one-tenth for 2D to one-third for 3D), and the number of views/phase encoding lines used for each time frame (160 versus 256). While the 2D radial images had slightly higher SNR compared with that of Cartesian, possibly due to the radial technique's robustness to motion, the 3D SNR measurements had substantially reduced SNR. We believe that the primary reason for the difference is the use of k-space

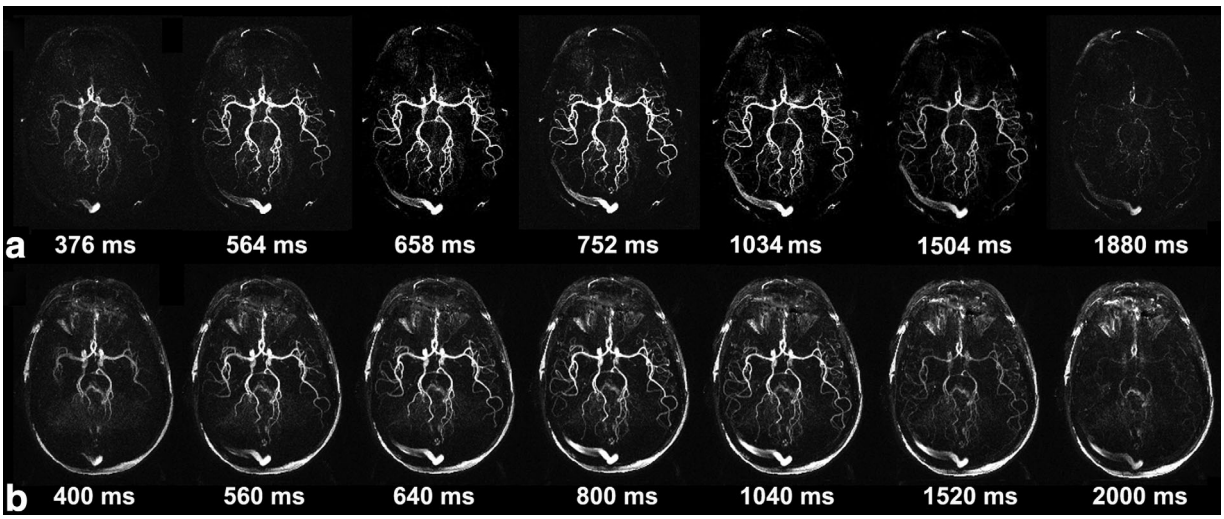

FIG. 5. Results from a 32-slice 3D data set showing seven temporal phases of stack-of-stars radial (**a**) and Cartesian (**b**) dMRA axial MIP images.

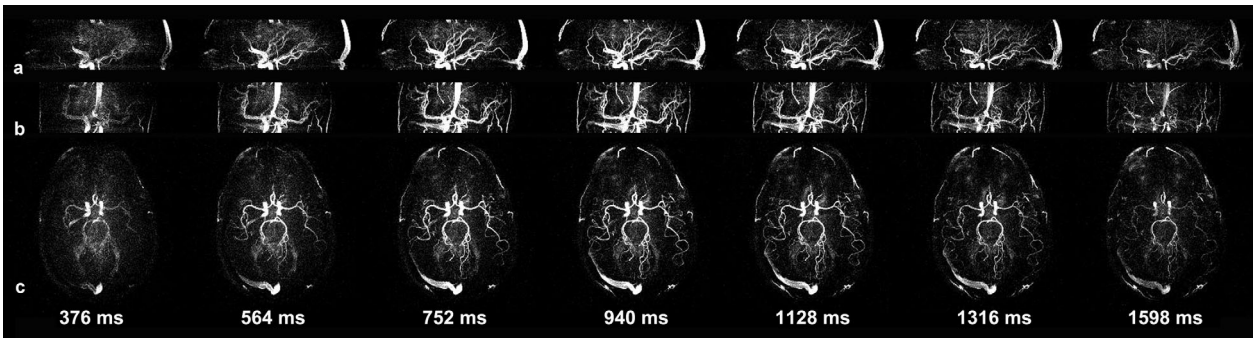

FIG. 6. MIP images of a 64-slice 3D stack-of-stars radial dMRA acquisition with 1 × 1 × 1mm^3 isotropic spatial resolution along sagittal, coronal and axial views of a healthy volunteer.

apodizing filters along the slice-encoding direction for standard online reconstructions, while no such filters were used for radial images processed offline. This is most evident when one compares the radial and Cartesian 3D images in the AVM patient (Fig. 8). It is quite clear that although the prescribed spatial resolutions were similar (1 × 1 × 1.5 versus 1.1 × 1.1 × 1.5 mm^3), one can readily see that the Cartesian images appear substantially more blurred, which is what is expected, along with increased SNR, when apodizing filters are used. The relative blurring also seems to be worse in the sagittal and coronal planes, supporting the idea that the lowpass filter is primarily along the slice direction, which leads to lower effective spatial resolution along the superior–inferior axis.

Advantages of Golden Angle Radial with KWIC

In this work, the golden angle was used to advance each subsequent view. The golden angle strategy provides more flexibility in achievable temporal resolution than previous equal angle strategies (bit-reverse or angle bisection (20)), albeit at a slight reduction in SNR (18). An interleaved multi-shot golden angle strategy was also

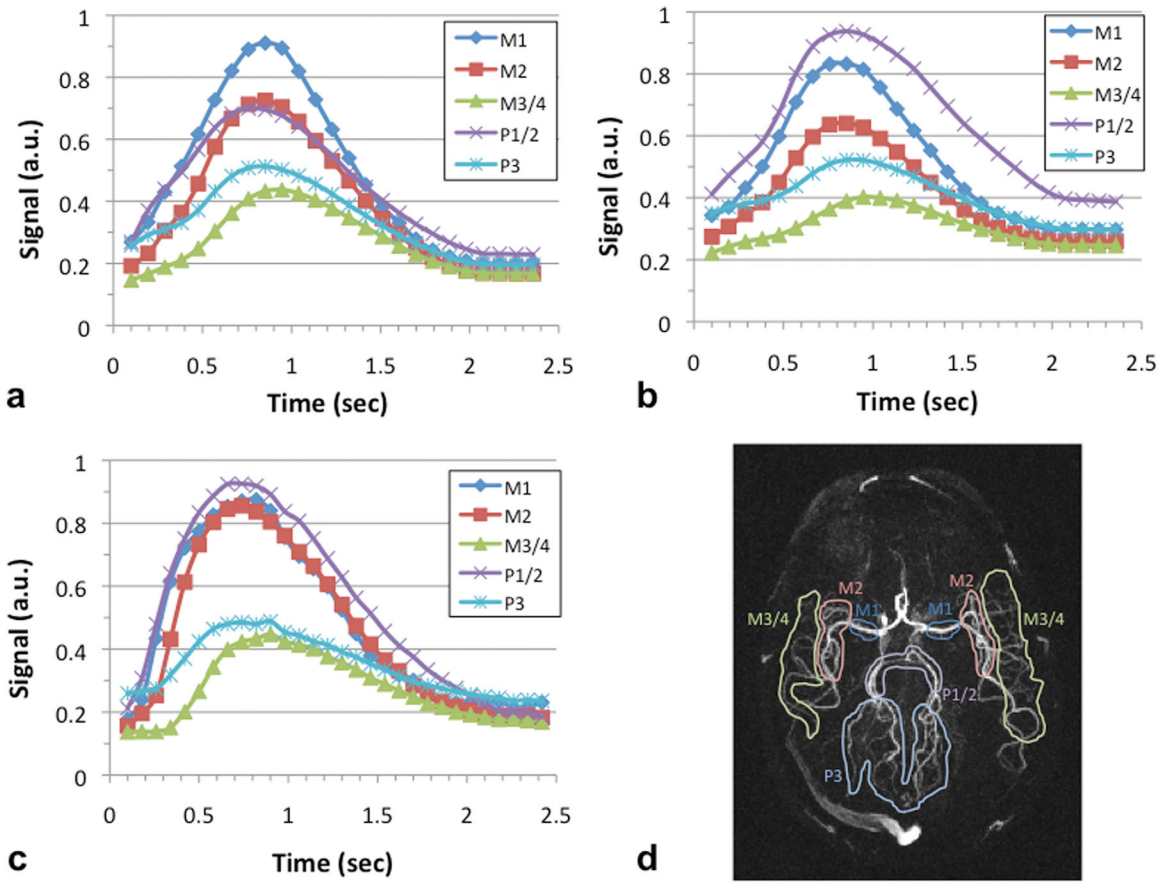

FIG. 7. Dynamic signal time course measured in the various arterial vessels of the brain of one of the volunteers for (**a**) 32-slice radial; (**b**) 64-slice radial; and (**c**) 32-slice Cartesian data sets. The time course signal was measured in various ROIs shown in (**d**). [Color figure can be viewed in the online issue, which is available at wileyonlinelibrary.com.]

Table 1
Comparison of Ratings (mean ± SD) of Image Quality between Three-Dimensional Radial and Cartesian dMRA Acquisitions[a]

	ACA	Left M1	Right M1	Left M2	Right M2	Left M3/4	Right M3/4	P1/2	P3
Radial	3.1 ± 0.8	4.0 ± 0.0	3.5 ± 0.8	4.0 ± 0.0	3.4 ± 1.1	3.8 ± 0.4	3.1 ± 0.9	3.9 ± 0.3	3.8 ± 0.4
Cartesian	2.8 ± 0.8	3.8 ± 0.5	3.7 ± 0.5	3.6 ± 0.5	3.5 ± 0.7	3.0 ± 0.9	2.3 ± 1.1	2.2 ± 1.1	2.2 ± 1.1
P value	0.28	0.08	0.91	0.09	0.52	0.052	0.20	0.16	0.03[b]

[a]1 = poor; 2 = moderate; 3 = good; 4 = excellent.
[b]$P < 0.05$ Wilcoxon signed rank two-sided.

proposed in this work for the purpose of increasing the number of central k-space views while keeping the temporal resolution constant at 100 ms. Higher number of interleaves then permits larger radius Nyquist rings in KWIC-filtered k-space, as well as smaller total temporal footprint for each time frame, yielding higher measurement accuracy (Fig. 2b). A second option one may consider with an interleaved acquisition is to increase the effective temporal resolution by keeping the number of views within each Nyquist ring constant. For example, with two interleaves, 20 views could encode k-space center (10 from each shot) while the effective temporal resolution is halved to 50 ms.

While the enhanced flexibility in temporal resolution is likely the biggest benefit of the golden angle scheme compared with the bit-reverse method, there are other attractive features that the former strategy provides. With golden angle view increment, the temporal window which encodes the k-space center could always be centered within the total temporal footprint of that time frame (the only exceptions are at the very beginning and end of the acquisition series). In other words, for our 160-view, KWIC reconstructed series, the central 20 views are temporally centered, with 70 views preceding and 70 views following those views encoding the more distant k-space regions. This is not the case with the bit-reversal method in which there will always be an imbalance with slightly greater contribution from either pre- or post-time periods depending on the time frame, and as with the golden angle strategy, higher temporal asymmetry at the beginning and end of the dynamic series. In addition, the manner in which the views are mapped in k-space is more

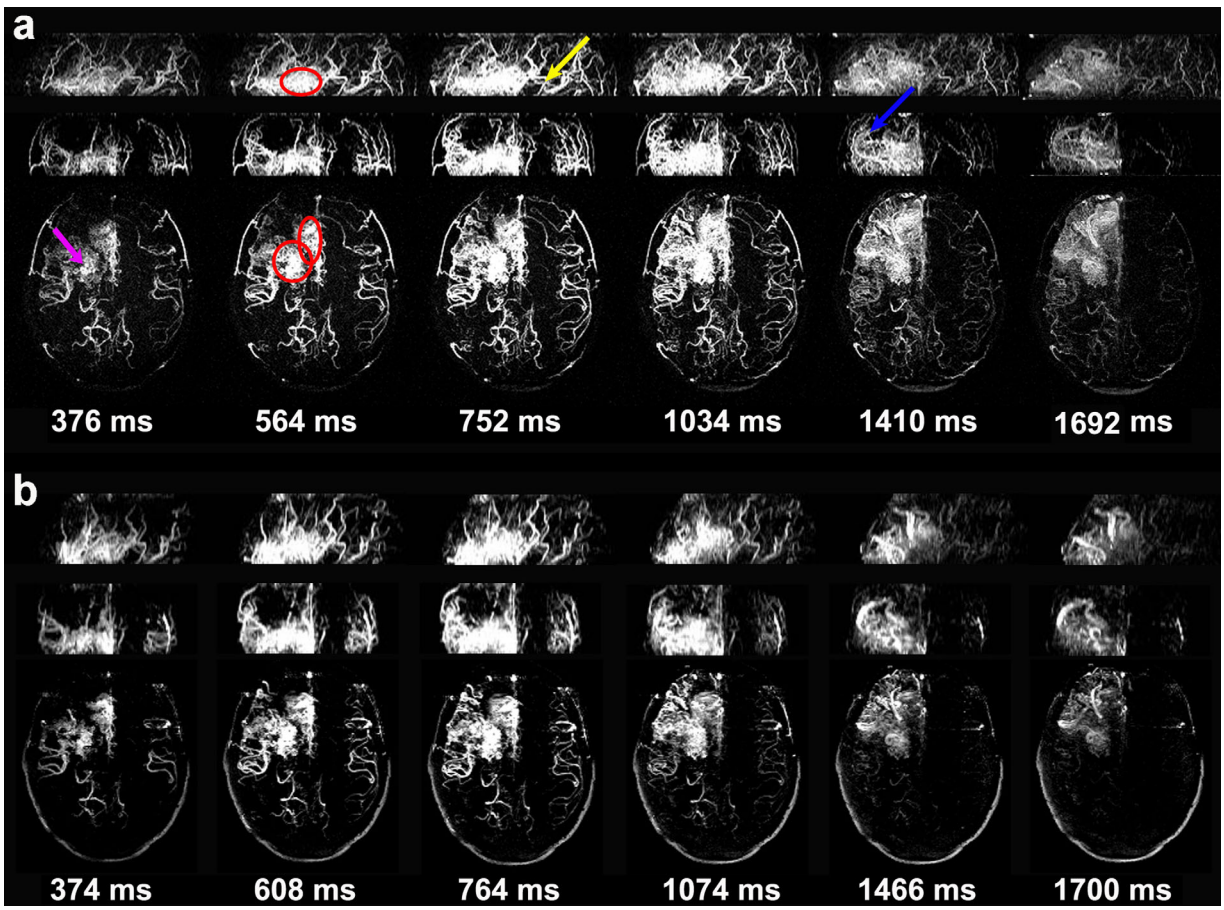

FIG. 8. MIP images of 3D stack-of-stars radial dMRA (**a**) and 3D Cartesian dMRA (**b**) along sagittal, coronal and axial views of the AVM patient (20 yrs, female). Red circles: AVM measuring approximately 6.1 × 4.9 × 4.9 cm; Pink arrow: Right MCA; Yellow arrow: Straight sinus; Blue arrow: Sagittal sinus. [MIP video files for both Cartesian and radial acquisitions for the AVM patient can be viewed in the Supplemental Information.]

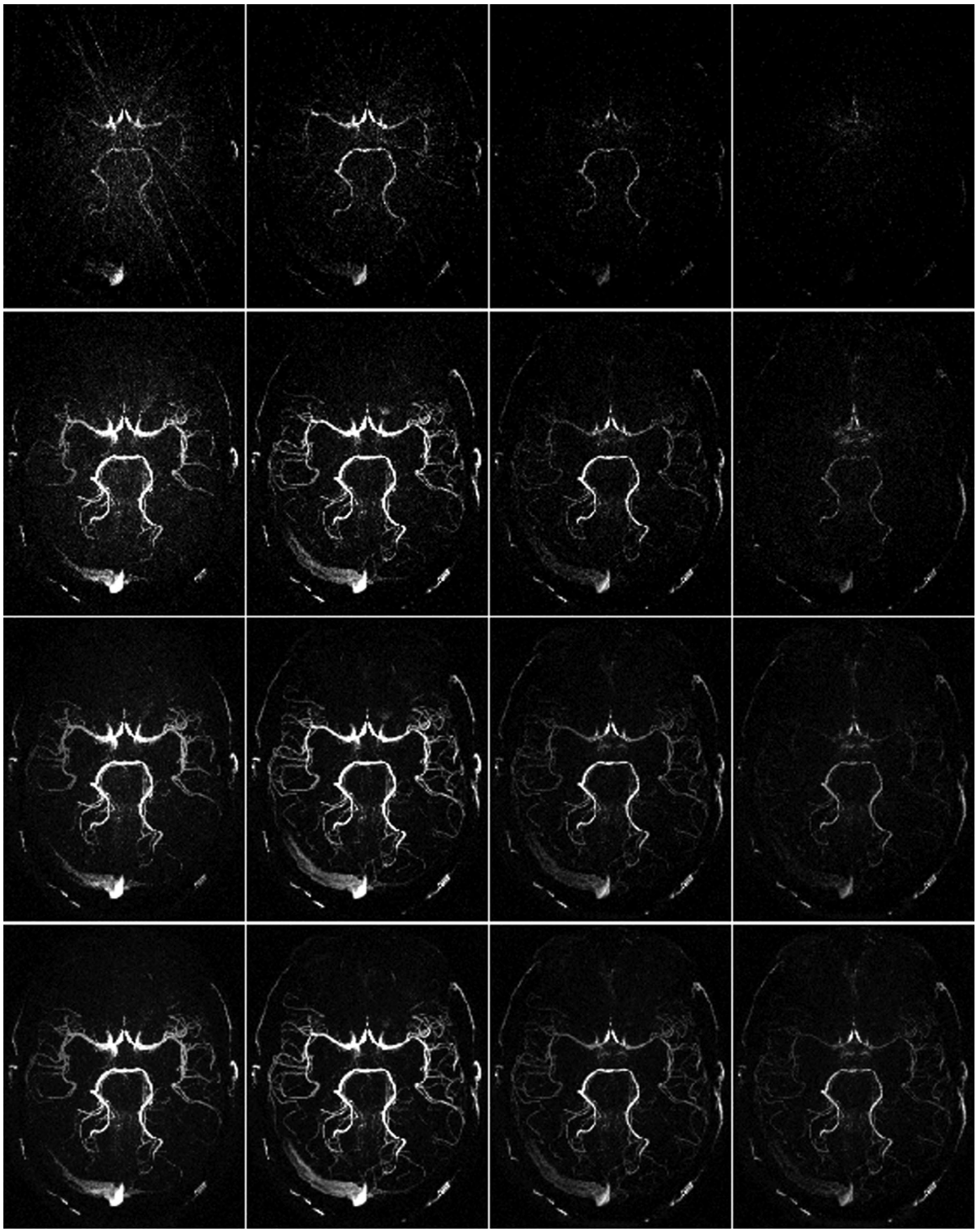

FIG. 9. MIP images of a 3D radial dMRA dataset of one of the healthy volunteers reconstructed with KWIC using 20 views at k-space center and different total views per time frame: (**a**) 20 total views; (**b**) 80; (**c**) 160; (**d**) 240.

consistent with the golden angle strategy, where the view order is mapped identically (apart from a rotation of all views) from one time frame to the next. With the bit-reversal method, the k-space mapping is not identical from frame to frame, potentially leading to slight signal intensity biases in dynamic curves (20).

Song and Dougherty (20) demonstrated in a simulation study that when the KWIC strategy is applied to a dynamic dataset comprised of rapidly changing signal, the temporal response is greatly improved compared with standard sliding window reconstruction which does not use KWIC. Although some measurement errors due to KWIC-induced temporal blurring are expected to increase in small or thin objects, errors were mostly small, on the order of 5% or less. In the current application as demonstrated in the simulation study, only when

the vessel size is small (less than 3 mm) does the error exceed 5%, and this only occurs for single-shot acquisition. As the temporal footprint of KWIC reconstruction diminishes with increasing number of shots, the errors become even smaller in multi-shot acquisitions.

Choice of Optimal Imaging Parameters

The 160 total views used for each KWIC time frame is well below what the Nyquist criterion demands. For a 256-point readout used in this work, approximately 400 views would be needed to fulfill Nyquist. However, the feasibility of attaining good image quality in MRA with undersampled radial acquisition has already been demonstrated, even with an undersampling factor exceeding a factor of 10 (5). The choice of 160 views for this work is as follows: In essence, we first decided to achieve a sufficiently high frame rate and decided on ~100 ms temporal resolution, leading to 20 views at k-space center for KWIC processing. We also wanted to minimize the total temporal footprint of each KWIC time frame, i.e., minimize the total number of views used for each frame, while maintaining sufficiently high image quality (high SNR and low streaking artifacts). Figure 9 shows several KWIC reconstructed time frames using 20 central views in conjunction with 20, 80, 160, or 240 total number of views per time frame. Based on visual inspection, it was decided that 160 views offered a good compromise between good image quality and small temporal footprint. Using fewer numbers of views yielded lower SNR and/or image streaking, while using larger number of views led to increased temporal blurring. Admittedly, the optimal number of views is largely subjective and may also depend on several factors, including the particular application or anatomy, specific scan parameters, and image SNR.

Although not explored in the present study, radial dMRA with KWIC offers additional flexibility that allows the reconstruction of several different image series with different spatial/temporal resolution tradeoffs—all from the same dynamic dataset. For instance, a neurosurgeon can first view a static MRA with high spatial resolution and high SNR based on all radial acquisitions, and then view high temporal frames of dMRA at the temporal resolution of his/her choice.

Alternative Strategies for Image Acceleration

In this work, the KWIC strategy was shown to be effective in drastically reducing the total scan time without significantly sacrificing spatial or temporal resolution. However, alternative strategies may also be considered for scan time reduction such as highly constrained back projection reconstruction (HYPR) (27). In HYPR, a high resolution composite image is generated from the full k-space data acquired throughout the whole (or part of the) acquisition window, whereas individual time frame images are constructed by multiplying the composite image with undersampled temporal weighting images (28–30). While HYPR can be effective in improving the effective temporal resolution, residual artifacts akin to temporal blurring can still occur (31,32), and methods have been developed to mitigate these artifacts (33). Alternatively, KWIC can be combined with parallel imaging methods, such as GRAPPA operator for wider radial bands (GROWL) (34).

Compressed sensing (CS) is another method that can potentially improve acquisition efficiency. CS is an iterative technique, which uses data fidelity and often one or more regularization terms, such as finite difference, to reconstruct images using limited data for each image. For dynamic series, one can incorporate spatial, temporal, or spatio-temporal combination in the regularization term, and previous reports have demonstrated some success (35–37). However, one of the biggest challenges of the CS strategy, in particular for dynamic imaging involving many time frames, is the reconstruction time, which can be prohibitive and preclude their use in routine clinical practice. The usage of multi-core processing with GPUs may yield more acceptable reconstruction times, and is currently being explored by several investigators (38–40).

Further Development of Noncontrast Dynamic MRA

ASL based noncontrast dMRA uses labeled blood as an endogenous contrast agent for visualizing the dynamic flow pattern. As demonstrated previously (41,42), the saturation effect of flowing spins is relatively small (<15%) as long as the flow velocity is greater than 2 cm/s. However, in older subjects and patients with cerebrovascular disorders there may be a greater reduction of dMRA signals, especially with a thick 3D imaging slab. This limitation may be circumvented by a novel dMRA approach termed multi-bolus TrueSTAR (43) in which a series of labeled boluses (using the STAR strategy) were carried out during the continuous multiphase TrueFISP readout with minimal disturbance of the steady-state signal, thereby forming a prolonged integrated bolus to enhance the dMRA signal. Cardiac gating can further be applied for dMRA to minimize the effect of cardiac pulsation, and may lead to a novel approach for estimating vascular compliance if dMRA acquisition is synchronized to the systolic and diastolic phases of the cardiac cycle (44). Finally, the above strategies (multi-bolus TrueSTAR and cardiac gating) can be combined with dynamic golden angle radial trajectory and KWIC filtering to improve imaging speed.

CONCLUSIONS

Our preliminary work demonstrates the feasibility of 2D and 3D golden angle radial acquisition scheme for noncontrast enhanced dynamic MRA. This work combines the reconstruction flexibility of the golden angle radial acquisition with KWIC temporal filtering to dramatically reduce the scan time compared with conventional methods, while achieving high spatial and temporal resolution. For the 2D single-shot implementation, a scan time that is only one-tenth of the standard Cartesian-based dMRA was achieved, without substantial temporal smoothing, while the scan time reduction was a factor of three for 3D. As a next step, the utility of dMRA with dynamic golden angle radial acquisition needs to be evaluated in clinical studies.

ACKNOWLEDGMENT

The authors thank Dr. Songlin Yu for his assistance with the evaluation of dMRA images in healthy volunteers.

REFERENCES

1. Willinsky RA, Taylor SM, TerBrugge K, Farb RI, Tomlinson G, Montanera W. Neurologic complications of cerebral angiography: prospective analysis of 2,899 procedures and review of the literature. Radiology 2003;227:522–528.
2. Korosec FR, Frayne R, Grist TM, Mistretta CA. Time-resolved contrast-enhanced 3D MR angiography. Magn Reson Med 1996;36:345–351.
3. Mistretta CA, Grist TM, Korosec FR, Frayne R, Peters DC, Mazaheri Y, Carrol TJ. 3D time-resolved contrast-enhanced MR DSA: advantages and tradeoffs. Magn Reson Med 1998;40:571–581.
4. Nael K, Michaely HJ, Villablanca P, Salamon N, Laub G, Finn JP. Time-resolved contrast enhanced magnetic resonance angiography of the head and neck at 3.0 tesla: initial results. Invest Radiol 2006;41:116–124.
5. Peters DC, Korosec FR, Grist TM, Block WF, Holden JE, Vigen KK, Mistretta CA. Undersampled projection reconstruction applied to MR angiography. Magn Reson Med 2000;43:91–101.
6. Summers PE, Kollias SS, Valavanis A. Resolution improvement in thick-slab magnetic resonance digital subtraction angiography using SENSE at 3T. J Magn Reson Imaging 2004;20:662–673.
7. Tsuchiya K, Aoki C, Fujikawa A, Hachiya J. Three-dimensional MR digital subtraction angiography using parallel imaging and keyhole data sampling in cerebrovascular diseases: initial experience. Eur Radiol 2004;14:1494–1497.
8. Gauvrit JY, Leclerc X, Oppenheim C, Munier T, Trystram D, Rachdi H, Nataf F, Pruvo JP, Meder JF. Three-dimensional dynamic MR digital subtraction angiography using sensitivity encoding for the evaluation of intracranial arteriovenous malformations: a preliminary study. AJNR Am J Neuroradiol 2005;26:1525–1531.
9. Gauvrit JY, Oppenheim C, Nataf F, et al. Three-dimensional dynamic magnetic resonance angiography for the evaluation of radiosurgically treated cerebral arteriovenous malformations. Eur Radiol 2006;16:583–591.
10. Noguchi K, Melhem ER, Kanazawa T, Kubo M, Kuwayama N, Seto H. Intracranial dural arteriovenous fistulas: evaluation with combined 3D time-of-flight MR angiography and MR digital subtraction angiography. AJR Am J Roentgenol 2004;182:183–190.
11. Mori H, Aoki S, Okubo T, et al. Two-dimensional thick-slice MR digital subtraction angiography in the assessment of small to medium-size intracranial arteriovenous malformations. Neuroradiology 2003;45:27–33.
12. Nagaraja S, Capener D, Coley SC, Lee KJ, Wilkinson ID, Kemeny AA, Griffiths PD. Brain arteriovenous malformations: measurement of nidal volume using a combination of static and dynamic magnetic resonance angiography techniques. Neuroradiology 2005;47:387–392.
13. Bi X, Weale P, Schmitt P, Zuehlsdorff S, Jerecic R. Non-contrast-enhanced four-dimensional (4D) intracranial MR angiography: a feasibility study. Magn Reson Med 2010;63:835–841.
14. Yan L, Wang S, Zhuo Y, Wolf RL, Stiefel MF, An J, Ye Y, Zhang Q, Melhem ER, Wang DJ. Unenhanced dynamic MR angiography: high spatial and temporal resolution by using true FISP-based spin tagging with alternating radiofrequency. Radiology 2010;256:270–279.
15. Yu S, Yan L, Yao Y, et al. Noncontrast dynamic MRA in intracranial arteriovenous malformation (AVM), comparison with time of flight (TOF) and digital subtraction angiography (DSA). Magn Reson Imaging 2012;30:869–877.
16. Xu J, Shi D, Chen C, Li Y, Wang M, Han X, Jin L, Bi X. Noncontrast-enhanced four-dimensional MR angiography for the evaluation of cerebral arteriovenous malformation: a preliminary trial. J Magn Reson Imaging 2011;34:1199–1205.
17. Lanzman RS, Kropil P, Schmitt P, et al. Nonenhanced ECG-gated time-resolved 4D Steady-state free precession (SSFP) MR angiography (MRA) for assessment of cerebral collateral flow: comparison with digital subtraction angiography (DSA). Eur Radiol 2011;21:1329–1338.
18. Winkelmann S, Schaeffter T, Koehler T, Eggers H, Doessel O. An optimal radial profile order based on the Golden Ratio for time-resolved MRI. IEEE Trans Med Imaging 2007;26:68–76.
19. Song HK, Dougherty L. k-space weighted image contrast (KWIC) for contrast manipulation in projection reconstruction MRI. Magn Reson Med 2000;44:825–832.
20. Song HK, Dougherty L. Dynamic MRI with projection reconstruction and KWIC processing for simultaneous high spatial and temporal resolution. Magn Reson Med 2004;52:815–824.
21. Valdueza JM, Balzer JO, Villringer A, Vogl TJ, Kutter R, Einhaupl KM. Changes in blood flow velocity and diameter of the middle cerebral artery during hyperventilation: assessment with MR and transcranial Doppler sonography. AJNR Am J Neuroradiol 1997;18:1929–1934.
22. MacIntosh BJ, Sideso E, Donahue MJ, Chappell MA, Gunther M, Handa A, Kennedy J, Jezzard P. Intracranial hemodynamics is altered by carotid artery disease and after endarterectomy: a dynamic magnetic resonance angiography study. Stroke 2011;42:979–984.
23. Kim SG. Quantification of relative cerebral blood flow change by flow-sensitive alternating inversion recovery (FAIR) technique: application to functional mapping. Magn Reson Med 1995;34:293–301.
24. O'Sullivan JD. A fast sinc function gridding algorithm for fourier inversion in computer tomography. IEEE Trans Med Imaging 1985;4:200–207.
25. Riffel P, Haneder S, Attenberger UI, Brade J, Schoenberg SO, Michaely HJ. Combined large field-of-view MRA and time-resolved MRA of the lower extremities: impact of acquisition order on image quality. Eur J Radiol 2012;81:2754–2758.
26. Sarty GE. Single TrAjectory Radial (STAR) imaging. Magn Reson Med 2004;51:445–451.
27. Mistretta CA, Wieben O, Velikina J, Block W, Perry J, Wu Y, Johnson K. Highly constrained backprojection for time-resolved MRI. Magn Reson Med 2006;55:30–40.
28. Mistretta CA. Undersampled radial MR acquisition and highly constrained back projection (HYPR) reconstruction: potential medical imaging applications in the post-Nyquist era. J Magn Reson Imaging 2009;29:501–516.
29. Johnson KM, Velikina J, Wu Y, Kecskemeti S, Wieben O, Mistretta CA. Improved waveform fidelity using local HYPR reconstruction (HYPR LR). Magn Reson Med 2008;59:456–462.
30. Wang K, Busse RF, Holmes JH, Beatty PJ, Brittain JH, Francois CJ, Reeder SB, Du J, Korosec FR. Interleaved variable density sampling with a constrained parallel imaging reconstruction for dynamic contrast-enhanced MR angiography. Magn Reson Med 2011;66:428–436.
31. Wu Y, Wieben O, Mistretta CA, Korosec FR. Evaluation of temporal and spatial characteristics of 2D HYPR processing using simulations. Magn Reson Med 2008;59:1090–1098.
32. Keith L, Rahimi M, Holmes J, Brittain J, Korosec F. Use of a computer-controlled motion phantom to investigate the temporal and spatial fidelity of HYPR processing. Magn Reson Med 2013. doi: 10.1002/mrm.24707.
33. O'Halloran RL, Wen Z, Holmes JH, Fain SB. Iterative projection reconstruction of time-resolved images using highly-constrained back-projection (HYPR). Magn Reson Med 2008;59:132–139.
34. Lin W, Huang F, Li Y, Reykowski A. GRAPPA operator for wider radial bands (GROWL) with optimally regularized self-calibration. Magn Reson Med 2010;64:757–766.
35. Smith DS, Welch EB, Li X, Arlinghaus LR, Loveless ME, Koyama T, Gore JC, Yankeelov TE. Quantitative effects of using compressed sensing in dynamic contrast enhanced MRI. Phys Med Biol 2011;56:4933–4946.
36. Adluru G, Awate SP, Tasdizen T, Whitaker RT, Dibella EV. Temporally constrained reconstruction of dynamic cardiac perfusion MRI. Magn Reson Med 2007;57:1027–1036.
37. Adluru G, McGann C, Speier P, Kholmovski EG, Shaaban A, Dibella EV. Acquisition and reconstruction of undersampled radial data for myocardial perfusion magnetic resonance imaging. J Magn Reson Imaging 2009;29:466–473.
38. Kim D, Trzasko J, Smelyanskiy M, Haider C, Dubey P, Manduca A. High-performance 3D compressive sensing MRI reconstruction using many-core architectures. Int J Biomed Imaging 2011;2011:473128.
39. Hansen MS, Sorensen TS. Gadgetron: an open source framework for medical image reconstruction. Magn Reson Med 2013;69:1768–1776.
40. Murphy M, Alley M, Demmel J, Keutzer K, Vasanawala S, Lustig M. Fast l(1)-SPIRiT compressed sensing parallel imaging MRI: scalable parallel implementation and clinically feasible runtime. IEEE Trans Med Imaging 2012;31:1250–1262.
41. Wu WC, Jain V, Li C, Giannetta M, Hurt H, Wehrli FW, Wang DJ. In vivo venous blood T1 measurement using inversion recovery true-FISP in children and adults. Magn Reson Med 2010;64:1140–1147.
42. Yan L, Li C, Kilroy E, Wehrli FW, Wang DJ. Quantification of arterial cerebral blood volume using multiphase-balanced SSFP-based ASL. Magn Reson Med 2012;68:130–139.
43. Yan L, Salamon N, Wang DJ. Time-resolved noncontrast enhanced 4-D dynamic magnetic resonance angiography using multibolus TrueFISP-based spin tagging with alternating radiofrequency (TrueSTAR). Magn Reson Med 2013. doi: 10.1002/mrm.24689.
44. Yan L, Smith R, Liu C, Kilroy I, Chen Y, Wang DJ. Assessing intracranial vascular compliance using dynamic arterial spin labeling. In Proceedings of the 21st Annual Meeting of ISMRM, Salt Lake City, Utah, USA, 2013. Abstract 106.